# Experimental and analytical study on tensile performance of perfobond connector in bridge engineering application

Liu, Yangqing; Xin, Haohui; Liu, Yuqing

**DOI**
10.1016/j.istruc.2020.11.045

**Publication date**
2021

**Document Version**
Final published version

**Published in**
Structures

Structures 29 (2021) 714–729

Contents lists available at ScienceDirect

Structures

journal homepage: www.elsevier.com/locate/structures

# Experimental and analytical study on tensile performance of perfobond connector in bridge engineering application

Yangqing Liu [a], Haohui Xin [a,b], Yuqing Liu [a,*]

[a] Department of Bridge Engineering, Tongji University, Shanghai, China
[b] Faculty of Civil Engineering and Geosciences, Delft University of Technology, Netherlands

ARTICLE INFO

*Keywords:*
Composite structures
Perfobond connector
Uplift tests
Tensile capacity and stiffness

ABSTRACT

In addition to general shear loading, perfobond shear connectors (PBLs) also undertake tensile uplift forces at the interfaces between steel parts and concrete components. The tensile behavior of PBLs is as significant as the shear behavior to the safety of composite bridge structures. For further evaluating the combined shear-tensile response of PBLs, it is necessary to first investigate the tensile mechanism of PBLs. Accordingly, uplift tests with three specimens under static and cyclic loading were performed to investigate the tensile behavior of PBLs. The test results showed that the breakouts of concrete blocks dominated the failure of PBLs in tension. The residual separation was negligible when the tension force was below 30 percent of the capacity. Subsequently, a detailed finite element (FE) model for the uplift test was established and validated based on the test results. The strain path inside concrete blocks was presented as a cup shape, whose dimension was relevant to the embedded depth of holes and the boundary conditions. Further, 360 FE models with varying hole diameters, perforated rebar diameters, embedded depths, and concrete strength were conducted to explain the tensile mechanism and provide databases for the theoretical analyses. The results showed that the diameter of perforated rebars was irrelevant to the tensile capacity and stiffness of PBLs, while both the tensile capacity and stiffness increased with the embedded depth and concrete strength. Besides, the tensile stiffness was also related to the hole diameter. Consequently, according to the forms of existing tensile capacity expressions for headed studs and Mindlin's solution, the equations for the tensile capacity and stiffness of PBLs were derived.

## 1. Introduction

Recently, perfobond shear connectors (PBLs) are increasingly applied to the interfaces between steel parts and concrete components [1]. There are two types of PBLs, namely perfobond ribs (holes on rib plates) and perfobond plates (holes located on main plates). As shown in Fig. 1(a), the PBL used in composite joints in hybrid girders is an example of perfobond plates, where the steel cell of the composite joint is plugged into the concrete girder. In this case, the PBLs are formed by employing perforated rebars inside the circle holes located on the steel plates. The axial force is transferred by the shear forces of PBLs [2]. By contrast, as one of the applications of perfobond ribs, Fig. 1(b) shows that the upper flanges of composite girders with corrugated webs usually use two arrays of perfobond ribs. They are designed to undertake the shear forces along the longitudinal direction of girders. However, on the condition of applying loads on the cantilever end of concrete decks, the PBLs also resist considerable tensile forces perpendicular to the upper flanges [3]. Fig. 1(c) and (d) show the perfobond ribs used in composite bridge towers and cable-tower composite anchorages, respectively. When the tower is under tremendous axial loads, the perfobond ribs are primarily used to resist the uplift force to prevent the buckling of steel plates [4]. The vertical component of the cable force applied on the bracket generates an additional bending moment [5], which causes some of the connectors to bear tensions. The tensile behavior of PBLs is as significant as the shear behavior to the structural safety. The designs of PBLs with no considerations of tensile performance are unsafe in some cases. For further evaluating the combined shear-tensile response of PBLs, it is necessary to first investigate the tensile mechanism of PBLs.

The investigations on the tensile behavior of PBLs are relatively limited as far as the authors' knowledge. Kim et al. [6] conducted pull-out tests with ten specimens to evaluate the tensile behavior of PBLs applied in pile caps. The test results showed that the embedded length significantly improved the bearing capacity of PBLs, while the effect of perforated rebars on that was limited. The effects of the hole diameters

* Corresponding author.
*E-mail address:* yql@tongji.edu.cn (Y. Liu).

https://doi.org/10.1016/j.istruc.2020.11.045
Received 21 March 2020; Received in revised form 27 September 2020; Accepted 16 November 2020
Available online 13 December 2020

and material properties on the tensile capacity of PBLs were unclear. Zhu et al. [4] investigated the pull-out performance of perfobond connectors with thin ribs. The test results showed that the thin-rib perfobond connectors could fail by the rupture of the underhole plate, and by the rupture of the hole-side plate. However, the tensile mechanism of regular perfobond connectors is still indistinct.

Hence, this paper aims to reveal the influential factors on the tensile performance and explain the tensile mechanism of PBLs. The uplift tests with three specimens under static and cyclic loading were performed to investigate the tensile behavior of PBLs. The test results, including the failure modes, tension-separation curves, the residual separations under stepped tensions, and the tension – rebar strain relationships were discussed in this paper. Subsequently, a detailed FEA model for the uplift test was established and validated by the test results. The tensile mechanism of each part was described through analyzing the strain path inside concrete blocks, the strain distribution of concrete dowels, and the stress on perfobond plates. Further, the parametric studies with 360 FE models were conducted to explain the tensile mechanism and provide databases for theoretical analyses. The considered parameters include the hole diameter, perforated rebar diameter, embedded depth of holes, and concrete strength. Consequently, according to the forms of existing tensile capacity expressions for headed studs, and Mindlin's solution [19], the equations for the tensile capacity and stiffness of PBLs were proposed.

## 2. Uplift tests

### 2.1. Test specimens

The uplift tests with three specimens were conducted to investigate the static and cyclic tensile behavior of PBLs. The three specimens are identical in terms of geometry dimensions and material properties, among of which PT-1 was loaded by a monotonic tensile force while PT-2 and PT-3 were loaded by a cyclic loading process.

Fig. 2 shows the configuration of the specimens, where $d$ and $d_s$ are the diameters of holes and perforated rebars. The web of the stiffed steel beam has a height of 400 mm to provide sufficient space to set the hydraulic jacks. The length and width of the steel beam are 700 mm and 500 mm, respectively. Under the steel beam, a perfobond plate with a size of 150 mm × 250 mm × 20 mm was longitudinally welded on the bottom flange. The diameters of circle holes and perforated rebars are 75 mm and 20 mm, respectively. Besides, the dimension of concrete blocks was designed as 700 mm × 500 mm × 500 mm. Distributed reinforcements with a diameter of 16 mm were embedded in the concrete blocks to avoid unexpected cracking of concrete. Before the concrete casting, all the steel plates were greased to diminish the impact of bond between steel and concrete.

### 2.2. Test setup and instrumentation

Fig. 3 shows the test setup and instrumentation of the uplift test. The

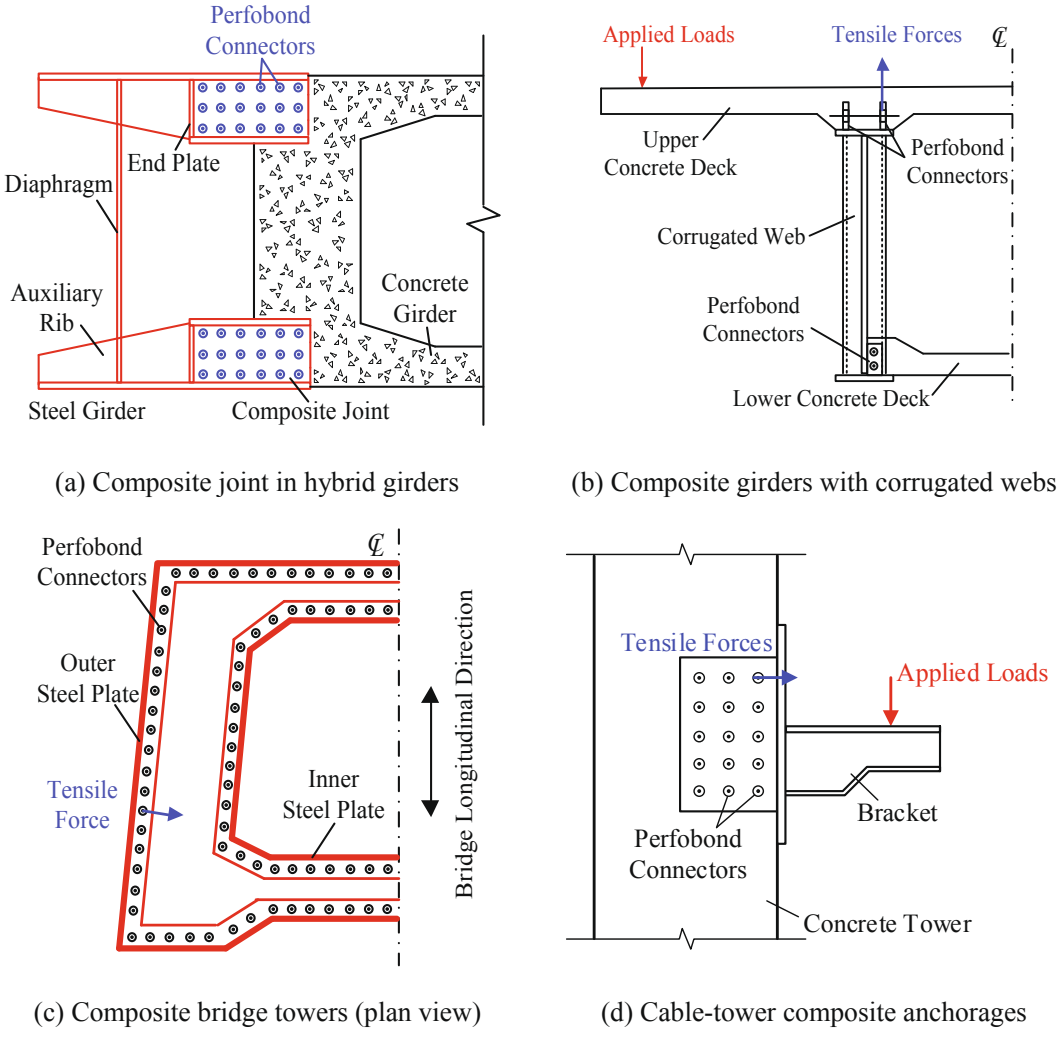


(a) Composite joint in hybrid girders

(b) Composite girders with corrugated webs

(c) Composite bridge towers (plan view)

(d) Cable-tower composite anchorages

**Fig. 1.** Applications of perfobond plates and perfobond ribs.

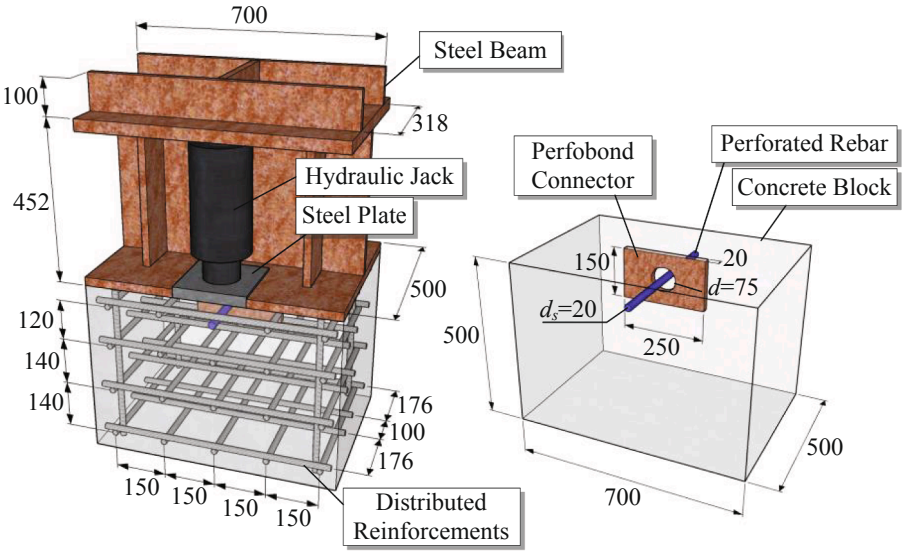


**Fig. 2.** Specimen configuration.

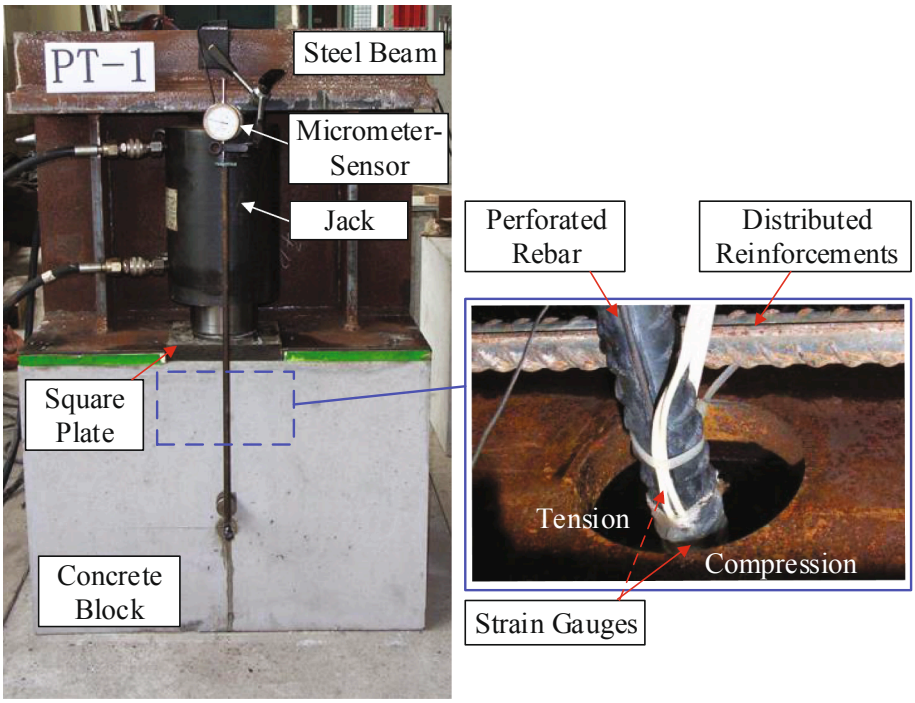


**Fig. 3.** Test setup and instrumentation.

specimens were loaded by two hydraulic jacks that are symmetric about the web of steel beams. In order to make the reaction force be uniformly distributed on the concrete block and prevent the concrete from local crushing, two square steel plates were placed between the jacks and the concrete block. The specimens were simply set on the lab floor.

To obtain the separations between the steel beam and the concrete blocks, two micrometer-sensors with the precision of 1/1000 mm were vertically mounted between the stiffeners of steel beams and concrete blocks on both front and back sides, as shown in Fig. 3. The other one was on the backside of specimens. Besides, to estimate the mechanical behavior and the contribution of perforated rebars, two strain gauges were respectively placed on the top and bottom edges of perforated rebars at the center of circle holes. Given the loading direction, RS-1 on the top edge was in tension, while RS-2 on the bottom edge was in compression.

The test loading started with the monotonic loading for PT-1 specimen, aiming to obtain the static ultimate tensile capacity of PBLs $T_u$. Subsequently, cyclic loading without reverse forces was carried out on PT-2 and PT-3. The cyclic load was incrementally increased from 0 to $1.0T_u$, with the increment of $0.1T_u$ per step.

### 2.3. Material properties

Concrete with the grade of C60 [11], which supposed the cubic compressive strength should be higher than 60 MPa, was employed for the specimens. In the process of casting concrete blocks, three groups of

nine concrete cubes with a size of 150 × 150 × 150 mm were fabricated to obtain the strength parameters of concrete. The tested cubic strength $f_{cu}$ at the age of 28 days was 62.5 MPa. According to CEB-FIP [12], the corresponding cylinder compressive strength $f_c$, tensile strength $f_t$, and elastic modulus $E_c$ were 50 MPa, 4.1 MPa, and 38.6 GPa, respectively.

The tensile tests on three groups of plate coupons and reinforcing rebars were conducted to get the strength of steel. The average yield strength and tensile strength of structural steel were 410 MPa and 545 MPa, respectively. The rebars had a yield strength of 382 MPa and a tensile strength of 547 MPa.

### 2.4. Test results

Table 1 summarizes the test results, where $T_u$ is the tensile capacity of PBLs; $k_T$ is the tensile stiffness of PBLs; $\Delta_p$ is the separation corresponding to the tensile capacity. Referred to the definition of shear stiffness of PBLs [7], the tensile stiffness is defined as the secant slope of the tension-separation curves where the separation equals 0.2 mm. Although the diameters of holes and perforated rebars of PBLs in this study were the same as those in the reference [8], the average tensile capacity is far lower than the shear capacity of PBLs. Compared with the static tensile capacity, the mean tensile capacity of PT-2 and PT-3 under cyclic loading decreased by 9%. It indicated that relatively large tension could introduce some damages to the tensile behavior of PBLs, but the influence was limited. By contrast, the effects of cyclic loading on the tensile stiffness were negligible, since the tension was relatively small in the early loading stage, and the damage caused by cyclic loading was inconsiderable. According to the test results shown in Table 1, no matter loaded by monotonic or cyclic tension, the peak separations were around 1 mm. Consequently, cyclic loading had minor effects on the tensile deformation behavior of PBLs.

Fig. 4 shows the failure modes of the uplift tests. Fig. 4(a) and (b) demonstrate that the majority of cracks were distributed on the top surface of concrete blocks. Cracking occurred along the edges of square plates closest to perfobond plates, where the reaction forces concentrated. Subsequently, the cracks radiantly developed outward from the region near perfobond plates. Fig. 4(c) illustrates the cracks with a considerable cracking width along the edges of the square plate. However, it's hard to find cracks in the region where square plates contacted with concrete blocks. The reason was that the compressive force given by jacks provided a significant confinement effect to the local concrete.

Fig. 4(e) shows the interior of concrete blocks after the tensile loading. As shown in the red box, the perforated rebar was separated from the concrete block. Even though the perforated rebar was bonded with concrete blocks in the modified push-out tests for the shear behavior of PBLs [9], perforated rebars were able to move along the transverse direction of rebars in tension. Lastly, Fig. 4(d) and (f) respectively show the deformation of perforated rebars and the shear fracture of concrete dowels. The perforated rebar presented the prominent bending deformation at the hole, which was different from the common failure modes of PBLs in shear. Additionally, the concrete dowels were sheared off, indicating that the dowels also undertook considerable shear forces as the separations increased since the reaction forces transferred by the square plates were close to the dowels.

Fig. 5 shows the tensile force-separation curves of the specimens. The envelopes of the curves of PT-2 and PT-3 were similar to the curve of PT-1, which consisted of three stages. The initial stage before 0.2 mm separation displayed in the embedded figure could be recognized as a linear part. Subsequently, the plastic stage started from around 0.2 mm separation and lasts to the peak separation, which was about 1 mm corresponding to the ultimate tensile capacity. Lastly, the failure stage began with the descending of the tensile force. Despite many cracks showing up on the top surface of concrete blocks, the reduction of tensile forces was slow. As shown in Fig. 4(d), the perforated rebars had yielded and developed plastic deformations before the breakouts of concrete. The high remained strength at the decreasing part indicated that perforated rebars could effectively improve the ductility of PBLs in tension.

Fig. 6 shows the residual separations of each load cycle for PT-2 and PT-3. It's noted that the residual separations were inconsiderable on the condition that the tensile forces were lower than $0.3T_u$. Besides, the increment of residual separations was relatively slow when the tensile forces were under $0.4T_u$. Therefore, $0.4T_u$ could be suggested as the design tensile strength of PBLs.

Fig. 7 shows the longitudinal strains of perforated rebars under cyclic loading, where RS-1 on the top edge was in tension, while RS-2 on the bottom edge was in compression. When the tension approached the tensile capacity, both of RS-1 and RS-2 were smaller than the yield strain of steel, and the perforated rebars were at the elastic state. The tensile strain was close to the compressive strain, indicating the bending dominated the deformation shape of rebars in this stage. However, at the early loading stage as shown in the figure on the right, the tensile strain was higher than the compressive strain. The shear stress transferred from the shear planes, which were along the plate surfaces, might limit the increase of the compressive strain of RS-2.

## 3. Numerical and parametric study

### 3.1. Numerical model

In this section, three-dimensional FE models for the uplift tests of PBLs were built by Abaqus / Explicit [13]. Fig. 8 presents the assembly of the numerical model, including the steel beam, concrete block, perfobond plate, perforated rebar, distributed reinforcements, square plates, and jack heads. Except for the distributed reinforcements and the jack heads, which were respectively simulated by the truss element T3D2 and the rigid element R3D4, all the components were modeled by the solid reduced integration element C3D8R. The model employed the consistent boundary conditions with the tests, including the contact between square plates and concrete blocks, the contacts between jack heads and square plates, and the fixed boundary conditions set at the reference points of the jack heads. For the static behavior, upward displacement loads were employed on the loading surfaces. By contrast, upward distributed tensile forces were applied on the loading surfaces for the cyclic loading.

Contact interactions were set at the interfaces between steel and concrete components, including the contact pairs between steel plates and concrete blocks, and the pairs between hole walls and concrete dowels. Also, the interfaces between perforated rebars and concrete blocks employed contact interactions since the perforated rebar visibly separated from the concrete block, as shown in Fig. 4(e). The normal property of the contact interactions was hard [13]. As regards the tangential property, the frictional coefficient was determined as 0.5. The reinforcements were embedded in the concrete blocks.

**Table 1**
Summary of test results.

| Specimen | $d$ (mm) | $d_s$ (mm) | $T_u$ (kN) | | $k_T$ (kN/mm) | | $\Delta_p$ (mm) | |
|---|---|---|---|---|---|---|---|---|
| | | | | AVG | | AVG | | AVG |
| PT-1 | 75 | 20 | 279.8 | 262.6 | 631.3 | 621.9 | 1.00 | 0.99 |
| PT-2 | 75 | 20 | 245.3 | | 609.5 | | 0.98 | |
| PT-3 | 75 | 20 | 262.7 | | 625.0 | | 0.97 | |

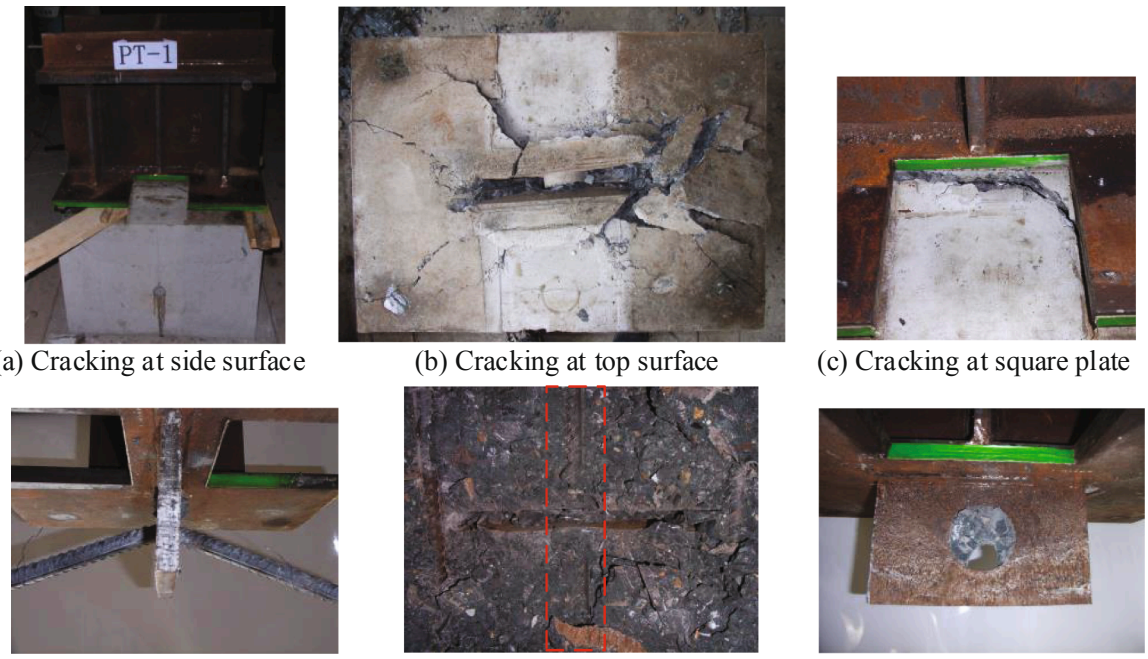


**Fig. 4.** Failure modes.

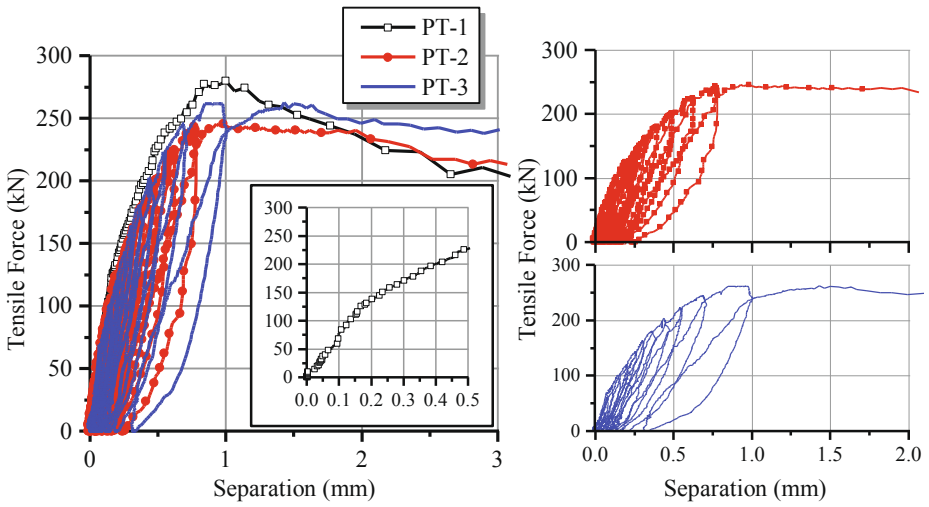


**Fig. 5.** Tensile force-separation curves.

### 3.2. Material property

The concrete constitutive law was described by the Concrete Damage Plasticity (CDP) model provided by Abaqus User's Manual [13]. The expansion angle was assumed as 37°; the flow potential eccentricity was 0.1; the ratio of biaxial to uniaxial compressive strength was 1.16; the ratio of the second stress invariant on the tensile meridian to that on the compressive meridian used the default value 0.67, and the viscosity coefficient was 0.

Fig. 9(a) shows the stress–strain curve and the damage parameter of concrete in compression. The ascending part of the compressive stress–strain was defined by Eqs. (1) to (3) provided in GB50010 [11], where $\varepsilon$ and $\sigma$ are the strain and stress at any point on the curve; $D_c$ is the uniaxial compressive damage evolution coefficient; $\varepsilon_c$ is the strain corresponding to the peak compressive stress, which is relevant with $f_c$ [11]; $\rho_c$, $n$ and $x$ are the dimensionless coefficients. The descending segment is a straight line, which ends at the point with 85% of the compressive strength [14]. The ultimate strain $\varepsilon_{cu}$ corresponding to the endpoint is related to $f_c$, according to GB50010 [11]. To further consider the cyclic tensile behavior of PBLs, the damage parameters for concrete were employed in this study. Referred to [8], the compressive damage parameter $d_c$ can be expressed as Eq. (4), where $\epsilon^{pl}$ is the plastic strain; $b_c$ is the ratio of plastic strain to inelastic strain, which equals 0.7 [8].

$$\sigma = (1 - D_c)E_c\varepsilon \tag{1}$$

$$D_c = 1 - \frac{\rho_c n}{n - 1 + x^n},\ x \leqslant 1 \tag{2}$$

$$\rho_c = \frac{f_c}{E_c\varepsilon_c},\ n = \frac{E_c\varepsilon_c}{E_c\varepsilon_c - f_c},\ x = \frac{\varepsilon}{\varepsilon_c} \tag{3}$$

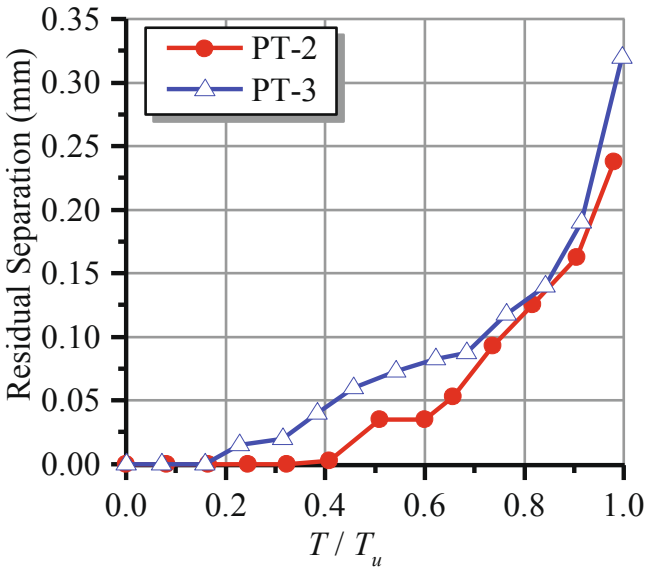


**Fig. 6.** Residual separations under stepped tensile forces.

$$d_c = 1 - \frac{\sigma}{E_c \varepsilon^{pl}(1/b_c - 1) + \sigma} \tag{4}$$

As regards the tensile behavior, the stress–strain curve and the damage parameter in tension are presented in Fig. 9(b). The tensile stress–strain curve was defined by Eqs. (5) to (7) provided in GB50010 [11]. Wherein $D_t$ is the uniaxial tensile damage evolution coefficient; $\varepsilon_t$ is the strain corresponding to the peak tensile stress, which is relevant with $f_t$ [11]; $\alpha_t$ is a coefficient related to the descending part of the stress–strain curve [11]; $\rho_t$ and $x$ are the dimensionless coefficients. Also, the tensile damage parameter $d_t$ was calculated by Eq. (8), where $b_t$ was taken as 0.7 determined through numerical tests.

$$\sigma = (1 - D_t) E_c \varepsilon \tag{5}$$

$$D_t = \begin{cases} 1 - \rho_t \left[1.2 - 0.2x^5\right], & x \leqslant 1 \\ 1 - \dfrac{\rho_t}{\alpha_t (x-1)^{1.7} + x}, & x > 1 \end{cases} \tag{6}$$

$$\rho_t = \frac{f_t}{E_c \varepsilon_t}, \quad x = \frac{\varepsilon}{\varepsilon_t} \tag{7}$$

$$d_t = 1 - \frac{\sigma}{E_c \varepsilon^{pl}(1/b_t - 1) + \sigma} \tag{8}$$

According to the test results, the failure of the specimens was irrelevant to the fracture of steel plates or rebars. Therefore, a trilinear elastic–plastic stress–strain relationship that was commonly used in numerical studies [8] was employed for the steel plates, perforated rebars, and distributed reinforcements. The yield plateau ranged from 1 to 10 times the yield strain, and the ultimate strain was equal to 6% [10].

### 3.3. Finite element results

#### 3.3.1. Comparison of tension-separation curves

Fig. 10(a) compares the tension-separation curve of PT-1 with the curve of the FEA model. For the static behavior, the numerical result well reflects the linear stage, the plastic stage, and the failure stage of PBLs in tension. The FEA model is feasible to predict the tensile capacity and initial tensile stiffness of PBLs. It's noticeable that the simulated tensile stiffness at the plastic stage is lower than that of test results. The reason might be that the bond or friction were underestimated in this numerical study, though the steel components were greased before casting of concrete. Fig. 10(b) shows the comparison of cyclic tension-separation curves from PT-3 and the numerical model. Overall, the FEA model can simulate the cyclic tensile performance of the specimen, including the entire cyclic loading process. The difference in the residual strength should be improved in the future works.

#### 3.3.2. Comparison of failure modes

Fig. 11 compares the simulated failure modes with the observed failures in the tests. As illustrated in Fig. 11(a), the equivalent plastic strain concentrated at the edges of square plates closest to the perfobond plate. Also, the cracks radiantly developed toward the edges of concrete

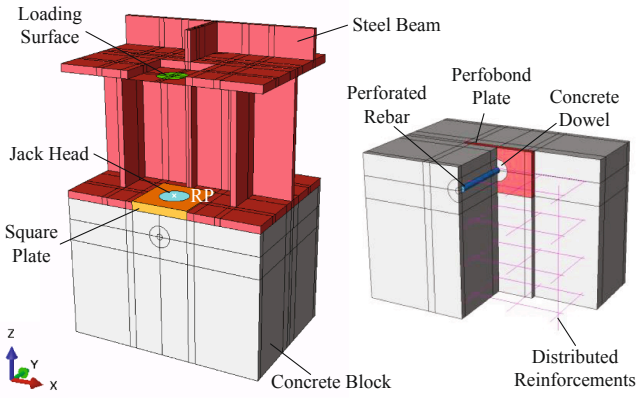


**Fig. 8.** Finite element model.

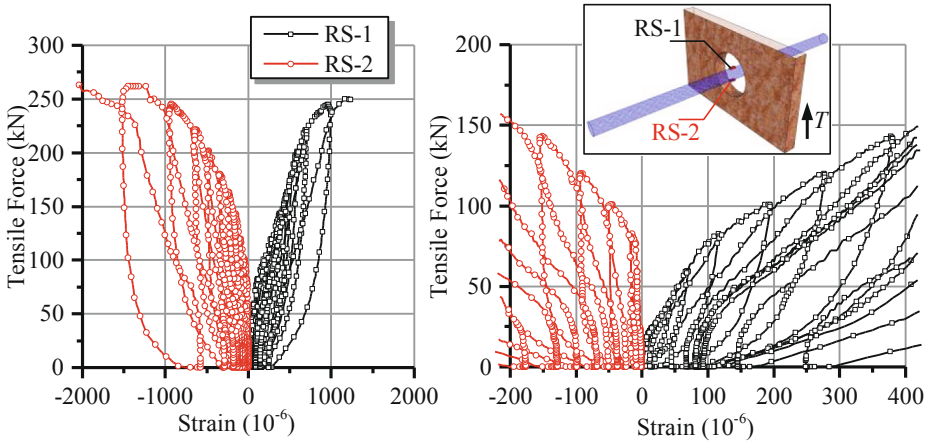


**Fig. 7.** Relationship between tensile forces and rebar strains.

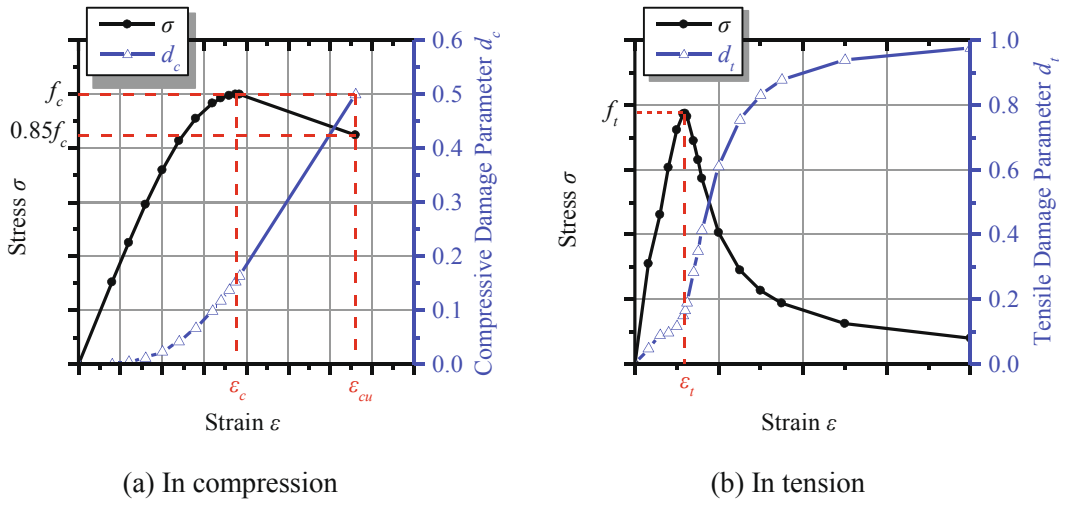


**Fig. 9.** Concrete constitutive laws.

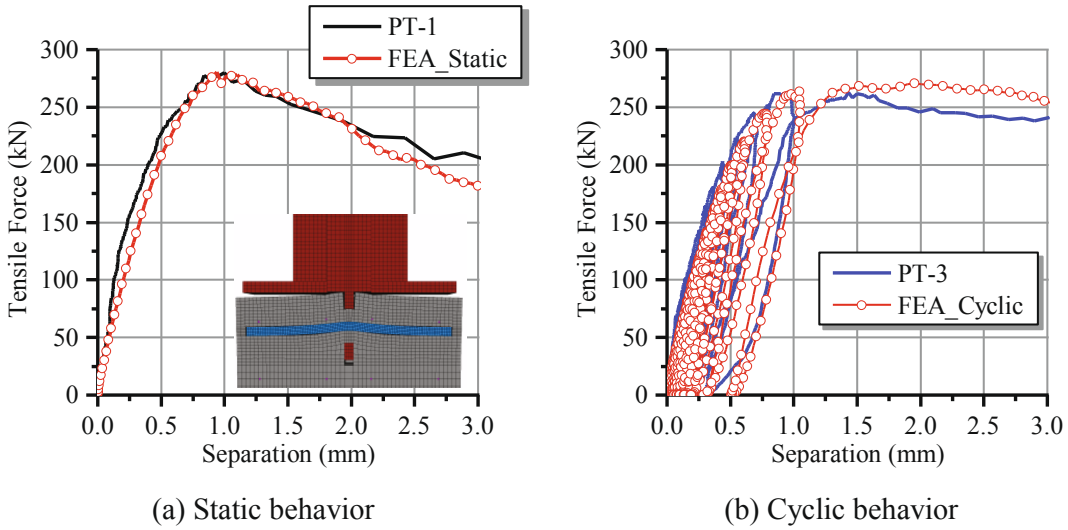


**Fig. 10.** Model validations.

blocks, which were consistent with the experimental cracking positions. The concrete dowels experienced large plastic strain with the increase of separations, the same as the fracture of concrete dowels in the tests. Compared with the test specimen, the FEA model generally repeated the cracking pattern of concrete components. As regards the perforated rebars, Fig. 11(b) depicts the deformation shape and Mises stress distribution of the perforated rebar of the numerical model. The local stress near the hole had exceeded the yield strength of rebars. The bending at the hole dominated the deformation shape of the perforated rebar, which was similar to the failure mode of lab tests. The reversal bending trend was caused by the constraint provided by square plates, which should be improved in the future works. Overall, the FEA model is valid to reveal the failure modes of PBLs in tension.

### 3.3.3. *Tensile mechanism*

Fig. 12 shows the distribution of equivalent plastic strains inside the concrete block under the tensile capacity. On the view cut of Plane YoZ, the plastic strains mainly distributed from the bottom of concrete dowel to the edge of the square plate where the reaction forces applied. By contrast, on the view cut of Plane XoZ, the strain path started from the middle position of the bottom of the concrete dowel and the perforated rebar and ended to the top surface of the concrete block above the edge of the concrete dowel. As demonstrated in the figure, the plastic strains mainly concentrated at the region in the shape of a cup. The size of the cup region might be related to the embedded depth of circle holes and the boundary conditions where the square plates were.

Fig. 13 presents the shear strains and the vertical strains in the concrete dowel under the tensile capacity. The shear strains symmetrically distributed on the two shear planes, and the value decreased with the distance to the bottom of the concrete dowel. It's noted that the shear strains were approximately uniform on the horizontal projection planes of the concrete dowel with the same depth. Fig. 13(b) illustrates that the vertical strains mainly concentrated at the lower half of concrete dowel, especially at the contact region between the hole wall and the bottom of the concrete dowel. The dimension of the concrete dowel affected the area with higher vertical strains, indicating that the diameter of dowels might be a factor on the tensile stiffness of PBLs.

Fig. 14(a) shows the magnitude and distribution of Mises stress on the perfobond plate when the applied load was equal to the tensile capacity. According to the stress contour, the stress primly distributed in the triangle region from the bottom edge midpoint to the top corners. The maximum Mises stress was far less than the yield strength of steel plates, indicating the perfobond plate was at the elastic state under the tensile capacity of PBLs. Fig. 14(b) presents the positions of the potential

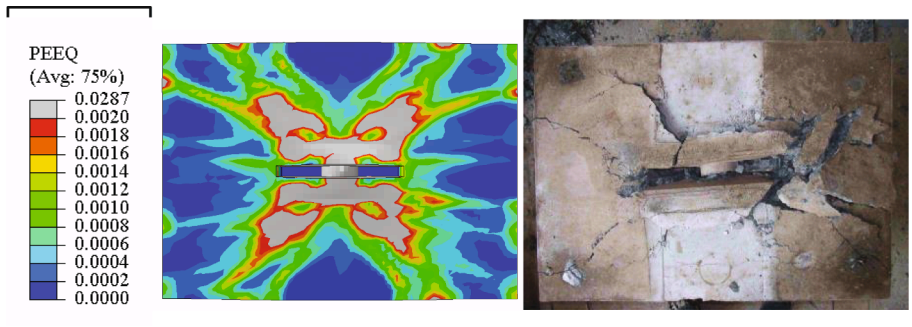


(a) Cracking of concrete block

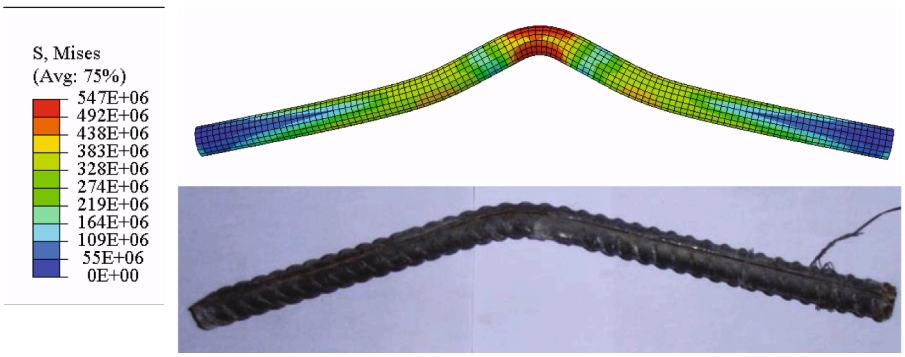


(b) Deformation of perforated rebar

**Fig. 11.** Comparison of failure modes.

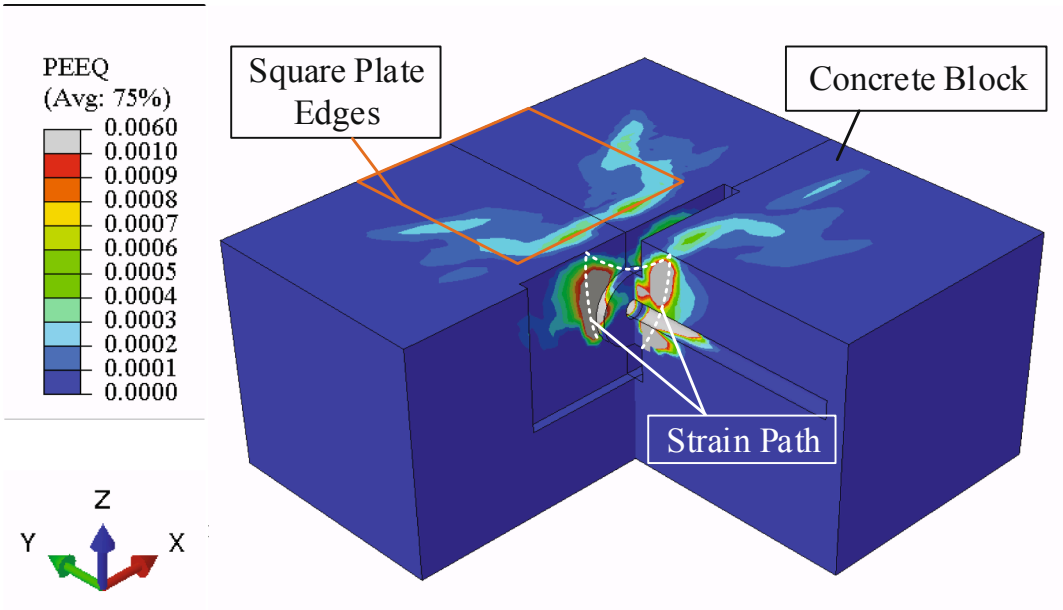


**Fig. 12.** Plastic strain distribution in concrete block.

shear fracture planes of perfobond plates. It's noticeable that the shear planes vertically located around the midpoints between the bottom and sides of the concrete dowel. Since the thickness of perfobond plates was 20 mm in this study, the shear stresses on the shear planes were below the shear strength of steel. However, designers should check the shear strength of perfobond plates, particularly on the condition of employing thin plates for PBLs.

### *3.4. Parametric study*

A sensitivity analysis was first performed to evaluate the effects of boundary conditions before the extensive parametric study. Fig. 15 shows the numerical results of models with the varying widths of concrete blocks as well as the positions of square plates, where the dimensions of square plates were kept as constants; *B* was the width of concrete block. As shown in the graph on the left, the tensile capacity

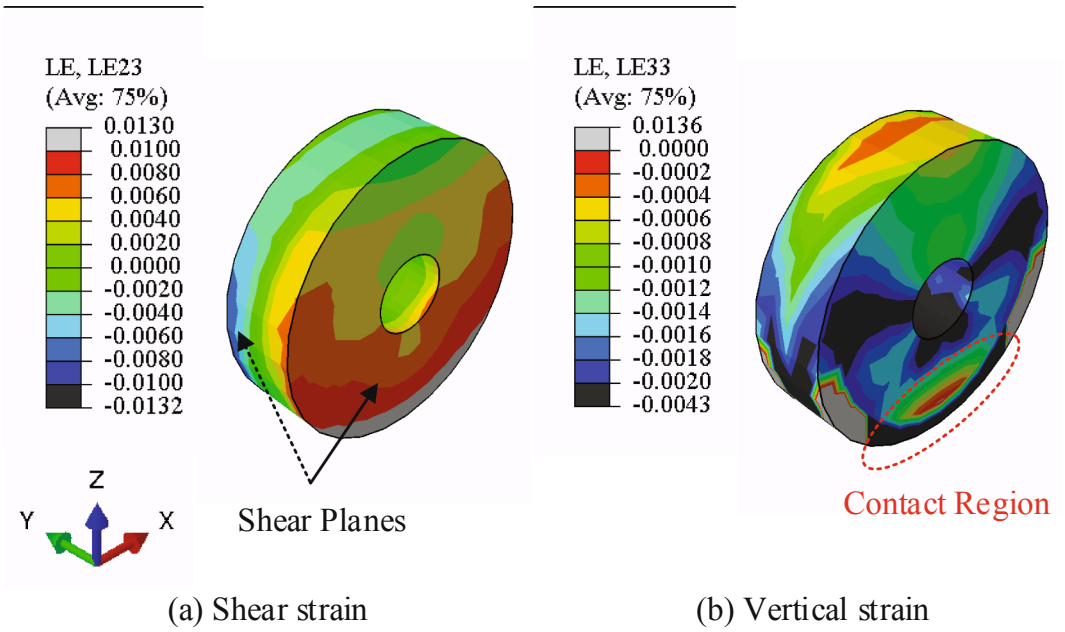


**Fig. 13.** Strains in concrete dowel.

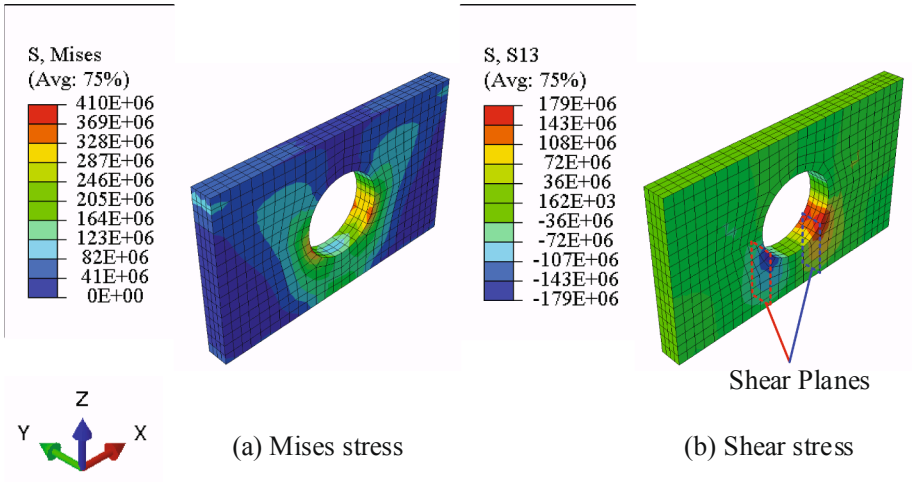


**Fig. 14.** Stress on perfobond plates.

dropped with the increase of distance between the square plate and the perfobond plate, since the restraint for concrete provided by the reaction forces decreased. However, the relative change in tensile capacity tended to decline as the larger distance was given. The impact of concrete width was negligible when $B$ was no less than 900 mm, indicating that the boundary condition under $B = 900$ mm was close to the practical free boundary without additional constraints. The plastic strain distribution (right side in Fig. 15) under the tensile capacities further supported the finding above. The incline angle and length of the strain path varied with the position of square plates, while they kept a similar pattern when $B =$ 900 mm and $B = 1100$ mm.

Subsequently, the effects of reinforcements on tensile behavior were investigated by varying the diameters of the rebars. Fig. 16 compares the tensile force-separation curves of the models with the different reinforcements embedded in the concrete blocks, where the diameters of the hole and the perforated rebar were 75 mm and 20 mm, respectively; the embedded depth of hole center was 75 mm; the concrete grade was C40. The reinforcements played a significant role in the tensile ductility of PBLs. Comparing the model using no reinforcements with the model employing 8 mm diameter rebars, both the tensile capacity and ductility improved. The increase in the diameter of the reinforcements enlarged the tensile capacity of PBLs. However, the relative increment dropped as the diameter rose because of the concrete performance degradation attributing stress concentration. Note that replacing the rebars with a diameter of 16 mm by the ones with a diameter of 25 mm, the tensile capacity only increased by 0.7%. Therefore, the diameter of reinforcements in the following analyses was set as 16 mm.

Thereafter, Fig. 17 shows the effects of the number of holes on the tensile behavior of PBLs, where $e$ is the center-to-center hole spacing. In this parametric analysis, $e$ equaled 100 mm or 80 mm; $d$ and $d_s$ equaled 60 mm and 20 mm, respectively; the embedded depth $u$ and the concrete grade were 50 mm and C40, respectively. The graph on the left shows that the tensile stiffness and capacity increased with the number of holes, and the relative increment was relevant to the hole spacing. The reason was that by using a larger hole spacing, the embedded depth of the second and the third holes increased. The graph on the right presents the plastic strain distribution inside the concrete blocks. It is found that the strain regions of the holes interacted with each other. An effective

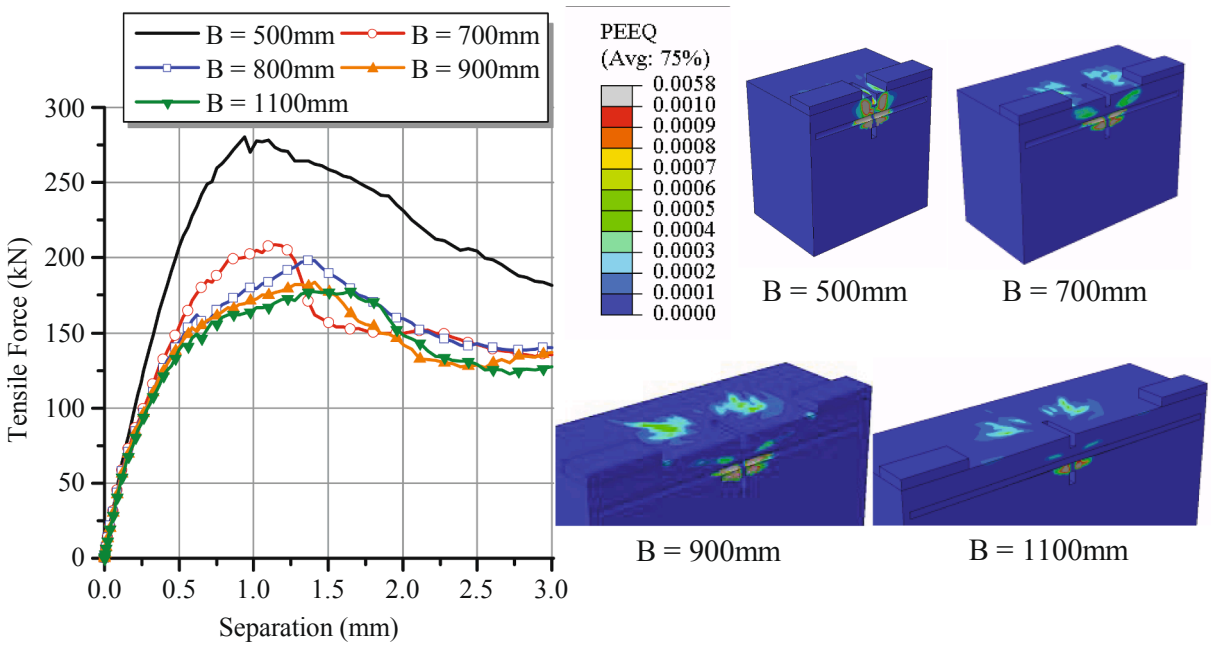


**Fig. 15.** Effects of boundary conditions.

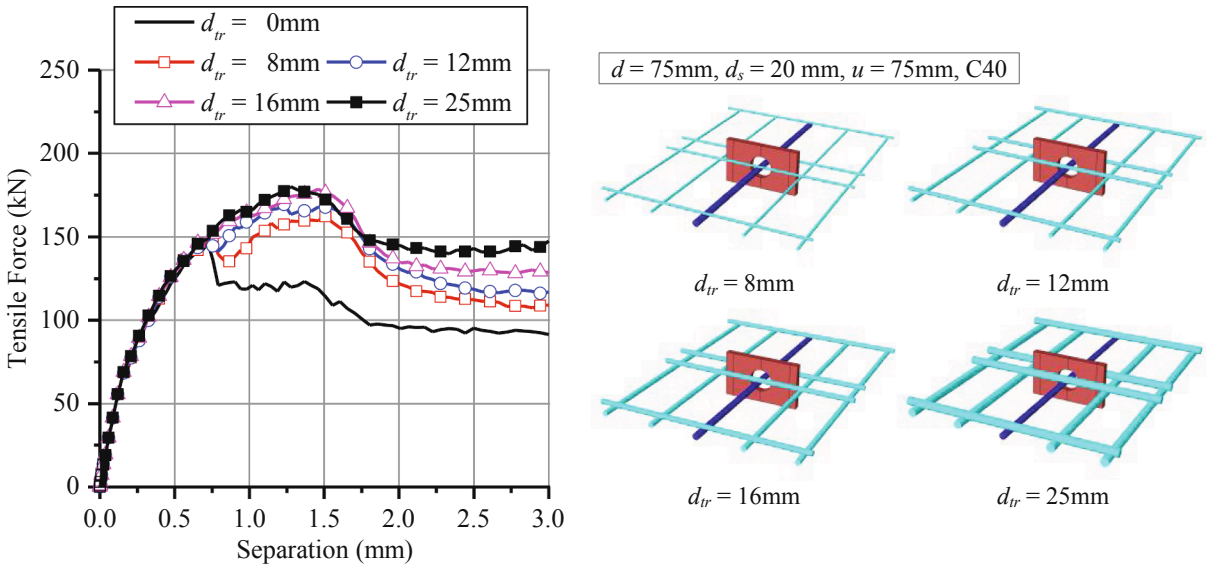


**Fig. 16.** Effects of reinforcements.

embedded depth $u_e$ of each hole should replace the absolute embedded depth $u$ in the analyses of the tensile capacity. Based on the numerical results, $u_e$ could be briefly defined as the distance between the hole center to the bottom of the adjacent concrete dowel, as shown in Fig. 17.

Fig. 18 shows the tension percentage of each hole during the tensile loading in the models with two and three holes where the hole spacing was 80 mm. The x-axis is the ratio of the total applied tensile force to the tensile capacity $T_u$. At the early loading stage, the first hole undertook more tension than the second and the third hole. The reason was that the holes had close tensile stiffness and the separation at the first hole was relatively larger than those at other holes. However, as the separation rose, the tensile stiffness of the holes with smaller embedded depths decreased, leading that the tension percentages of the third and the second hole significantly increased. The detailed investigation on the effects of the number of holes and the hole spacing on the tensile performance of PBLs will be presented in the future works.

The discussions above focus on the tensile mechanism of PBLs. For further exploring the tensile behavior and obtaining the database for theoretical analyses, a parametric study with 360 models was carried out by using the validated FE model. The considered parameters included the diameter of circle holes, diameter of perforated rebars, embedded depth of hole center, and concrete grade. Table 2 illustrates the range of parameters, where the concrete grade followed the definition in CEB-FIP MC2010 [12]. On the consideration of practicability, the diameters of perforated rebars always changed to be suitable for the hole diameter [8], and rebars with three different diameters were employed for one definite hole. For instance, for the hole with 50 mm diameter, the perforated rebars had the diameters of 16, 18, and 20 mm. Consequently, the width of concrete blocks was taken as 900 mm to reduce the confinement effects provided by reaction forces, which was close to the real boundary condition in applications of PBLs.

Fig. 19 shows the partial representative results of the parametric

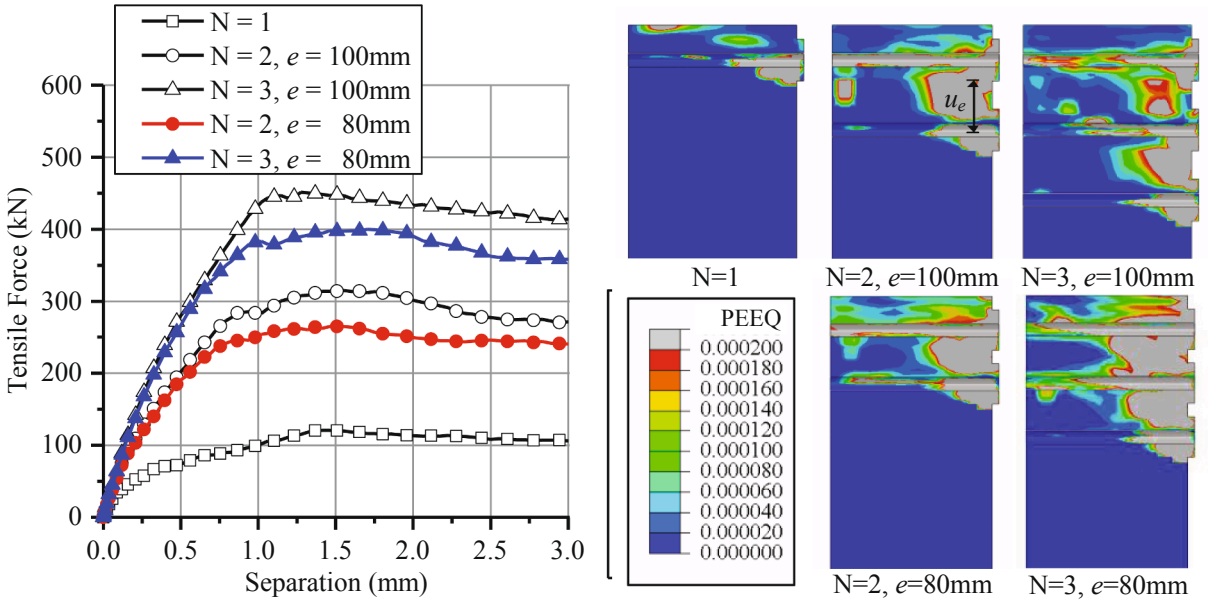


**Fig. 17.** Effects of the number of holes.

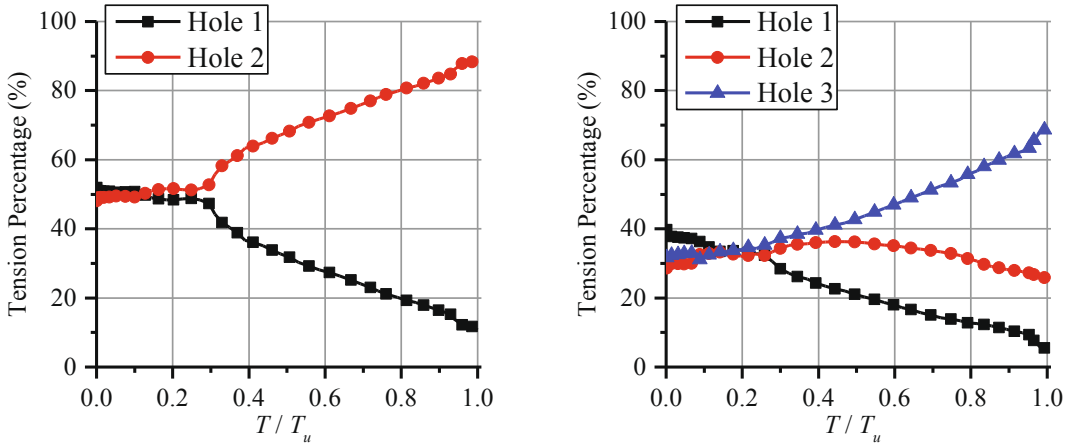


**Fig. 18.** Tension percentage of each hole.

**Table 2**
Range of considered parameters.

| Parameters | Range |
|---|---|
| Diameter of concrete dowel $d$ (mm) | 40, 50, 60, 75, 90 |
| Diameter of perforated rebar $d_s$ (mm) | 14, 16, 18, 20, 22, 25, 28 |
| Embedded depth of hole center $u$ (mm) | 50, 75, 100, 150, 200, 250 |
| Concrete grade | C30, C40, C50, C60 |

study, reflecting the impacts of the four parameters on the tensile capacity and stiffness of PBLs. Fig. 19(a) shows the tension-separation curves of the models with varying embedded depths, where the diameters of the circle hole and perforated rebar were 60 mm and 20 mm, and the concrete grade was C50. The embedded depth was the major influential factor on the tensile performance, including the tensile capacity, tensile stiffness, and tensile ductility. The tensile capacity increased with the embedded depth. Also, the difference in the tensile strength gradually decreased as the embedded depth rose. The numerical results showed that the model with an embedded depth of 50 mm presented better ductility than the models with the embedded depths of 75 mm, 100 mm, and 150 mm. The reason was that the perforated rebar could effectively prevent the perfobond plate from completely separating from the concrete block when the embedded depth was very small. The yielding of rebars occurred so that the PBLs with shallow embedded depths showed the fair ductility. By contrast, the models with medium embedded depths held a broader region of plain concrete, which enlarged the tensile capacity of PBLs but presented the brittle failure mode.

The occurrence of the ultimate tensile strength of PBLs was prior to the yielding of perforated rebar, resulting in the dramatic drop of the residual strength. Further, when the embedded depth was no less than 200 mm, the plain concrete could provide sufficient tensile strength before the yielding of perforated rebar. Thus, the models presented good ductility again. Fig. 19(b) and (c) present the effects of embedded depth and concrete compressive strength on the tensile capacity and stiffness. Both of the tensile capacity and stiffness increased with the concrete strength. The tensile stiffness was also significantly influenced by the embedded depth on the condition that the embedded depth was smaller than 100 mm. In contrast, the effect was negligible when that was larger than 100 mm.

Fig. 19(d) shows the tension-separation curves of the models with varying diameters of circle hole, where the diameter of perforated rebar

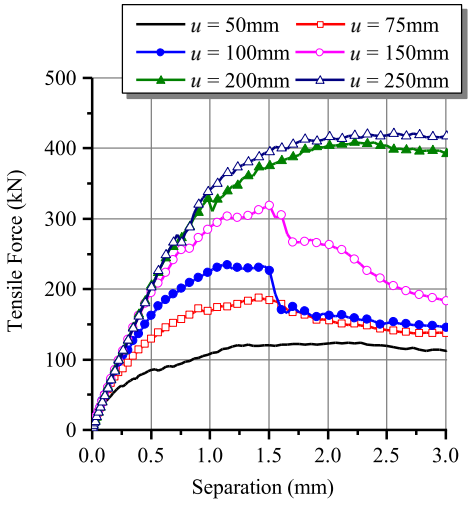


(a) Tension-separation curves with varying $u$

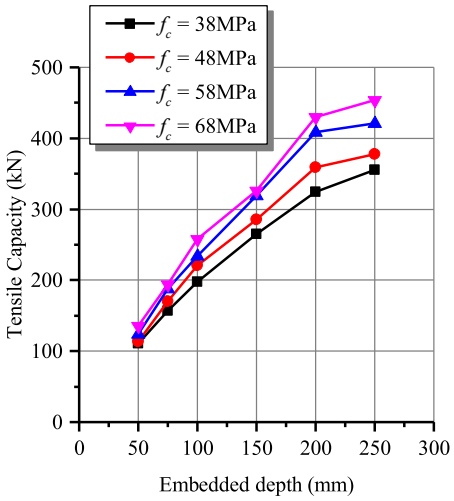


(b) Effects of $u$ and $f_c$ on tensile capacity

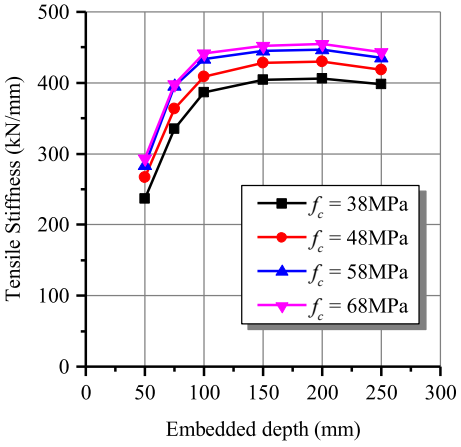


(c) Effects of $u$ and $f_c$ on tensile stiffness

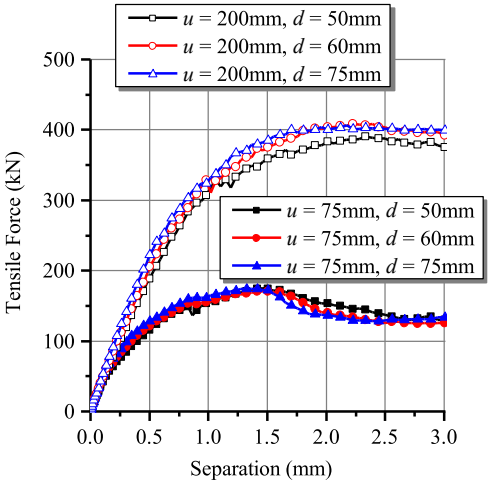


(d) Tension-separation curves with varying $d$

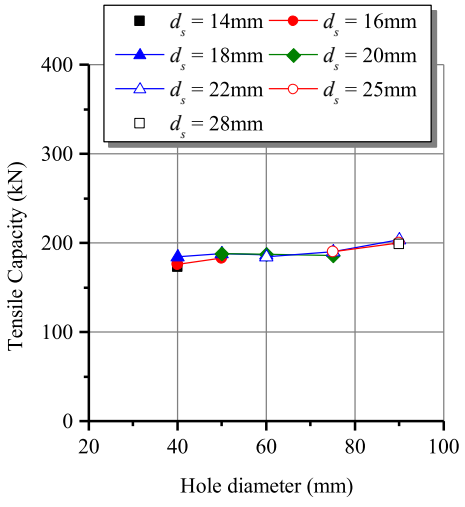


(e) Effects of $d$ and $d_s$ on tensile capacity

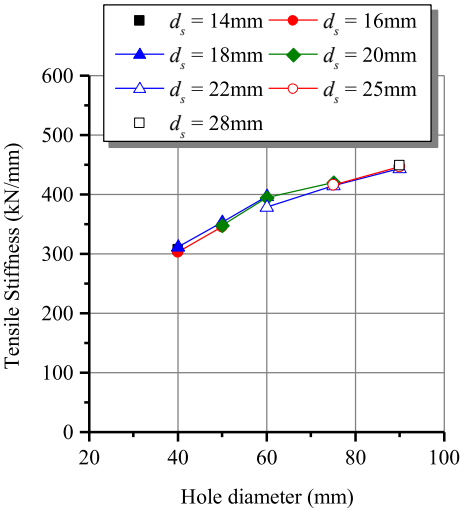


(f) Effects of $d$ and $d_s$ on tensile stiffness

**Fig. 19.** Results of parametric study.

was 20 mm, and concrete grade was C50. It's noted that the models with different hole diameters and the same embedded depth had similar curves, especially for the models with the smaller embedded depth. By using the practically representative parameters and boundaries, the concrete breakouts dominated the failure mode of the models, resulting in that the hole diameter performed a slight impact on the tensile capacity. Fig. 19(e) and (f) depict the effects of hole diameter and perforated rebar diameter on the tensile strength and stiffness, respectively. The tensile capacity was irrelevant to the diameter of perforated rebar, which could be explained that it's the concrete block instead of the dowel mattered the tensile strength. However, the tensile stiffness increased with the increment of hole diameter, because the hole dimension directly affected the contact area between hole walls and concrete dowels at the early loading stage.

To explain the above statements thoroughly, Fig. 20 describes the plastic strains inside the concrete blocks of four representative models under the tensile capacity, where the concrete grade was C50. By comparing Fig. 20(b) with 20(a), the increase of the embedded depth of concrete dowel enlarged the region of concrete in tension so that the tensile capacity and stiffness increased. However, the distributions of plastic strains in Fig. 20(a), (c), and (d) were almost the same, indicating that the variations of hole diameters and perforated rebar diameters were inconsiderable to the ultimate tensile capacity of PBLs.

## 4. Analytical equations

### 4.1. Tensile capacity of PBLs

According to the results of the parametric study, the major influential factors on the tensile capacity of PBLs are the embedded depth of concrete dowels and the strength of concrete. By contrast, the increase of the diameter of circle holes inefficiently enlarges the ultimate tensile force, and the influence of the diameter of perforated rebar on the tensile capacity is negligible. As mentioned, the cases that perfobond plates yield or fracture around the holes or fillet welds are out of the scope of this study. In this section, the existing tensile capacity equations [15–17] for headed stud connectors corresponding to the failure mode of concrete breakouts are referred to and discussed. Further, the tensile capacity expression for PBLs is proposed.

By carrying out tensile tests on headed shear studs, McMackin et al. [15] investigated the effects of edge distance, stud diameter, and embedded depth on the tensile behavior of headed shear studs. Based on the test results, the tensile capacity Eq. (9) for stud connectors was recommended, where $T_{cb}$ is the tensile capacity for the failure mode related to concrete breakouts; $d_h$ is the diameter of stud head; $h_{ef}$ is the effective embedded depth, which is the distance from the bottom surface of studs to the top surface of concrete blocks; $f_c$ is the cylinder compressive strength of concrete.

The expression contains the square root of the cylinder strength of concrete and the square of embedded depth. Additionally, the tensile capacity is affected by the diameter of the stud head. PCI 5th [16] includes Eq. (10) which has a similar form to Eq. (9) to evaluate the tensile capacity of headed studs. The only difference is the coefficient.

$$T_{cb} = 0.272\sqrt{2}\pi(d_h + h_{ef})h_{ef}\sqrt{f_c} \tag{9}$$

$$T_{cb} = 1.05(d_h + h_{ef})h_{ef}\sqrt{f_c} \tag{10}$$

Considering fracture mechanics concepts, ACI 318-08 [17] assumes a concrete failure prism with an angle of approximately 35° [18] and provides Eq. (11) for the concrete breakout strength of a single headed stud. $\psi_{ed}$ and $\psi_c$ are respectively the modifiers taking the edge distance and concrete cracking into account. The breakout strength is related to the embedded depth to the power of 1.5, as well as the square root of concrete strength.

$$T_{cb} = 10\psi_{ed}\psi_c h_{ef}^{1.5}\sqrt{f_c} \tag{11}$$

According to the expression forms and the analyses on the parametric study above, the tensile capacity equation of PBLs is proposed as Eq. (12), where $T_u$ is the tensile capacity; $d$ and $u$ are the diameter of circle holes and the embedded depth of the hole center, respectively. The coefficients in the equation are determined by regression analyses based on the FEA results of 360 models. Fig. 21 compares the calculated tensile capacity by Eq. (12) with the numerical results, where the coefficient of determination is 0.98. The mean value and the standard deviation of the ratios of calculated results to numerical results are 0.99 and 0.07, respectively.

$$T_u = 0.87(0.25d + u)^{\frac{3}{4}}\sqrt{f_c} \tag{12}$$

### 4.2. Tensile stiffness of PBLs

For exploring the deformation behavior and tension distribution of steel–concrete interfaces, the simplified force model is presented and further used to derive the equation for tensile stiffness of PBLs in this section. Under the tensile loading condition, the applied load is mainly resisted by concrete dowels and perforated rebars. The lower half of the

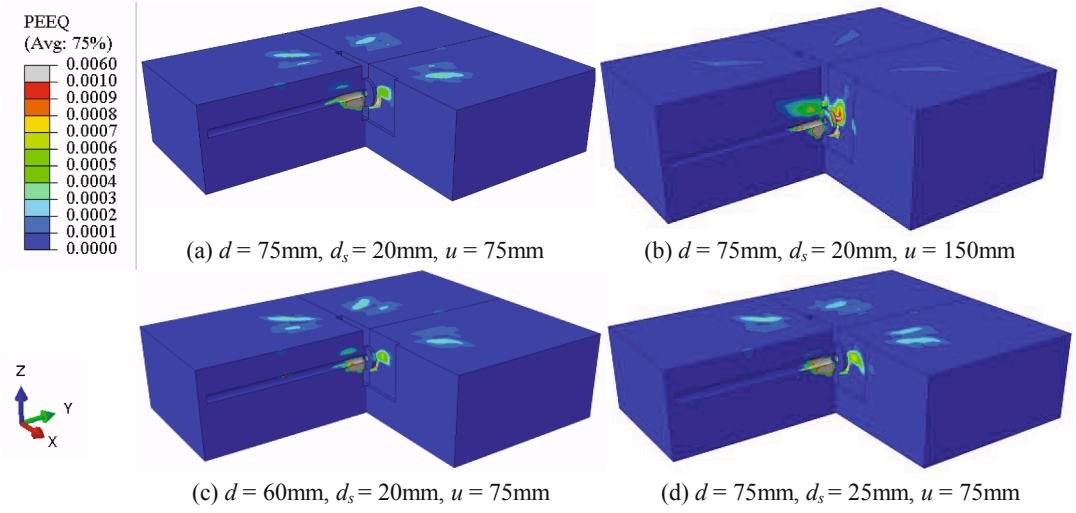


(a) $d$ = 75mm, $d_s$ = 20mm, $u$ = 75mm (b) $d$ = 75mm, $d_s$ = 20mm, $u$ = 150mm

(c) $d$ = 60mm, $d_s$ = 20mm, $u$ = 75mm (d) $d$ = 75mm, $d_s$ = 25mm, $u$ = 75mm

**Fig. 20.** Tensile mechanism of perfobond connectors.

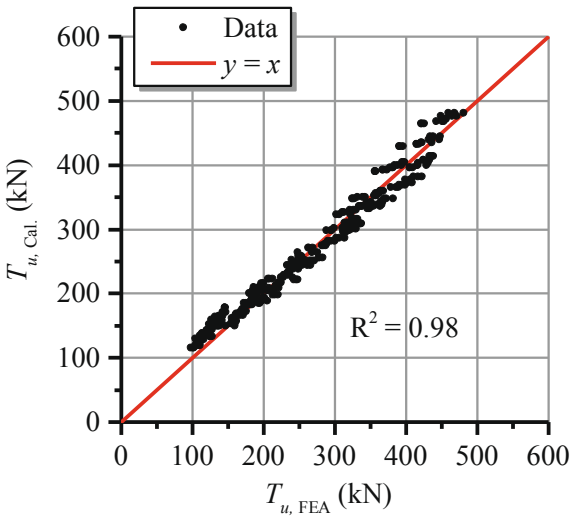


**Fig. 21.** Validation of tensile capacity expression.

hole wall is in close contact with concrete dowels. At the initial elastic stage, the force model can be regarded as applying a concentrated force in a semi-infinite elastic space.

Fig. 22 shows the global coordinate system of the mechanical model, where $O$ is the origin of the system; the continuous elastic medium is at $z \geq 0$; $O^F$ is the point applied the concentrated load P, and $O^M$ is the mirror point of $O^F$ about Plane XoY. The point A with the coordinate of (x, y, z) is any point in the semi-infinite space. $R_1$ and $R_2$ are the distance from A to $O^F$ and $O^M$, respectively. The task is to find the displacement at any point in the space. For this problem, Mindlin's solution provides the expression for the displacement of A [19], as shown in Eq. (13), where $v$ and $G$ are the Poisson's ratio and shear modulus of the elastic medium.

$$w = \frac{P}{16\pi G(1-v)}\left[\frac{3-4v}{R_1} + \frac{8(1-v)^2-(3-4v)}{R_2} + \frac{(z-c)^2}{R_1^3} + \frac{(3-4v)(z+c)^2-2cz}{R_2^3} + \frac{6cz(z+c)^2}{R_2^5}\right] \tag{13}$$

To simplify the derivation of the tensile stiffness of PBLs, the following assumptions are claimed:

(1) Steel and concrete are at elastic states;
(2) Assuming the stress and displacements are uniform along with the thickness of perfobond plates;
(3) Ignoring the effects of bond and friction at the interfaces between steel plates and concrete.

The separation $\Delta_T$ is defined as the displacement difference between the hole center and the semi-infinite space, which can effectively avoid

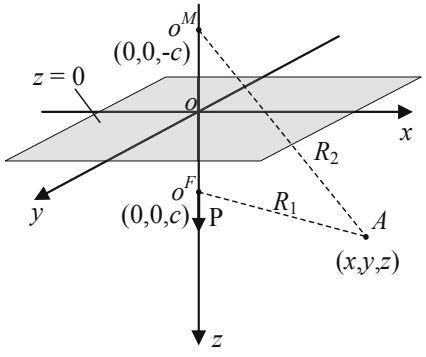


**Fig. 22.** Mindlin's solution in a semi-infinite solid.

the local singularity of Mindlin's solution. Also, the tensile stiffness $k_T$ is defined as the ratio of the tensile force $T$ to the separation $\Delta_T$. According to the parametric study results, the influence of perforated rebars on the tensile stiffness is inconsiderable and taken into account by adding fitting coefficients. Since the effects of plate thickness are neglected, the problem can be reduced to a plane problem. Fig. 23(a) shows the simplified force model of PBLs applied tensile forces in the global coordinate system, where the x-axis is the top surface of concrete blocks, and the concentrated load P is on the z-axis.

For facilitating the derivation process, a local polar coordinate system is built at the hole center $O'$, as shown in Fig. 23(b). The degree corresponding to the lower half of the hole wall ranges from 0° to 180°. In addition, it is supposed that the tensile force $T$ is evenly distributed along with the projection of circle holes. Thus, the distributed load $q$ is:

$$q = T/d \tag{14}$$

Pick a small segment of circular arc on the lower edge of the hole, as shown in Fig. 23(b). The vertical resultant force P on the arc segment is:

$$P = q\sin\theta r\mathrm{d}\theta = \frac{T\sin\theta}{2}\mathrm{d}\theta \tag{15}$$

$R_1$, the distance between the hole center $O'$ and the loading point $O^F$, is always kept as $r$, the hole radius. Also, $R_2$, the distance between the hole center $O'$ and the mirror point $O^M$, can be expressed by $u$ and $r$ in Eq. (17). Based on the nature of the expression, the value of $R_2$ is between $2u$ and $2u + r$. On the concern of facilitating the subsequent integral calculations, $R_2$ is simplified as Eq. (19) since the embedded depth $u$ is usually relatively larger than the hole radius $r$.

$$R_1 = r \tag{16}$$

$$R_2 = \sqrt{(2u + r\sin\theta)^2 + r^2\cos^2\theta} = \sqrt{4u^2 + 4ur\sin\theta + r^2} \tag{17}$$

$$2u < R_2 \leqslant 2u + r \tag{18}$$

$$R_2 = 2u + r \tag{19}$$

In the coordinate system above, the distance between the arc segment $O^F$ and x-axis can be written as Eq. (20). The z coordinate of the hole center $O'$ is $u$. According to Eq. (13), (15), (19) and (20), the displacement at the hole center $O'$ caused by the load P applied at the arc segment can be written as Eq. (21).

$$c = u + r\sin\theta \tag{20}$$

$$\mathrm{d}\Delta_T = \frac{T\sin\theta\mathrm{d}\theta}{32\pi G(1-v)}\left[\frac{3-4v+\sin^2\theta}{r} + \frac{8(1-v)^2-(3-4v)}{2u+r} + \frac{(3-4v)(2u+r\sin\theta)^2-2u(u+r\sin\theta)}{(2u+r)^3} + \frac{6u(u+r\sin\theta)(2u+r\sin\theta)^2}{(2u+r)^5}\right] \tag{21}$$

Further, $\mathrm{d}\Delta_T$ is integrated along the lower edge of the hole. The Poisson's ratio of the semi-infinite space is taken as the concrete Poisson's ratio. Substitute $v = 0.2$ and get:

$$\Delta_T = \int_0^{\pi} \mathrm{d}\Delta_T \tag{22}$$

$$\Delta_T = \frac{13T}{Gr}\frac{0.55u^5 + 1.96u^4r + 2.45u^3r^2 + 1.43u^2r^3 + 0.4ur^4 + 0.044r^5}{(2u+r)^5} \tag{23}$$

The molecular part of Eq. (23) is a fifth-order expansion form of binomial. The dimensionless coefficients are introduced to simplify Eq. (23).

$$\Delta_T = \frac{13T}{Gr}\left(\frac{\alpha u + \beta r}{2u+r}\right)^5 \tag{24}$$

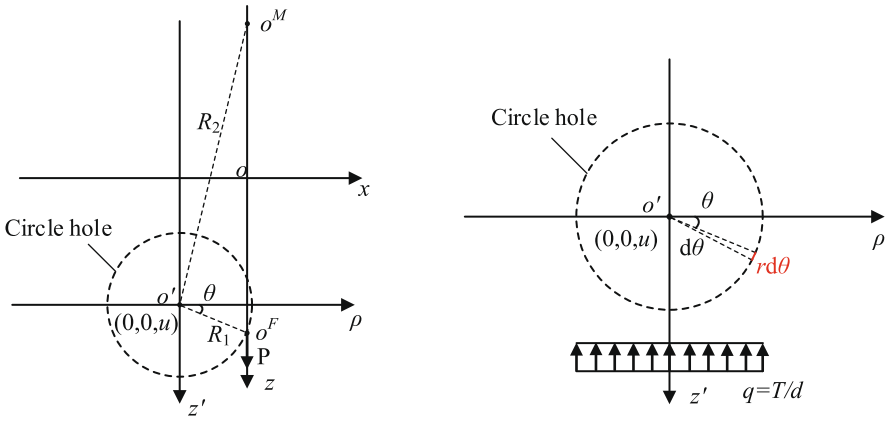


(a) Global coordinate system (b) Local polar coordinate system

**Fig. 23.** Simplified force models.

Finally, according to the definition of the tensile stiffness $k_T$, the expression of $k_T$ is written as Eq. (26), wherein $u_0$ is the effective embedded depth; $\alpha$ and $\beta$ are obtained by regression analyses based on the results of the parametric study.

$$k_T = \frac{T}{\Delta_T} = \frac{Gr}{13}\left(\frac{2u+r}{\alpha u+\beta r}\right)^5 \tag{25}$$

$$k_T = 0.0217E_c r\left(1 + \frac{2u_0}{2u_0+d}\right)^5 \tag{26}$$

$$\begin{cases} u_0 = u\ , & u \leqslant 100 \\ u_0 = 100\ , & u > 100 \end{cases} \tag{27}$$

Fig. 24 compares the calculated results by Eq. (26) with the FEA results. The coefficient of determination is 0.97. The mean value and the standard deviation of the ratios of calculated stiffness to numerical stiffness are 1.01 and 0.05, respectively.

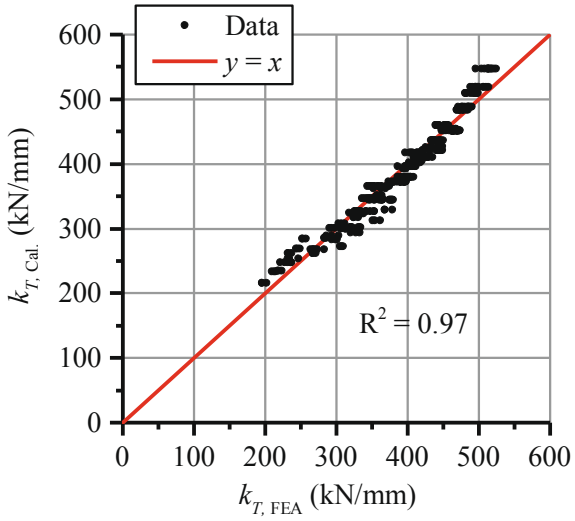


**Fig. 24.** Validation of tensile stiffness expression.

## 5. Conclusions

This paper documented uplift tests of PBLs under static and cyclic loading. The failure modes, tension-separation curves, residual separations under stepped tensions, and tension-rebar strain relationships were discussed. Subsequently, a detailed FE model for the uplift tests was established and validated by the test results. Further, 360 extended FEA models with varying hole diameters, perforated rebar diameters, embedded depths, and concrete strength were conducted to reveal the tensile mechanism. Finally, the equations for the tensile capacity and stiffness of PBLs were proposed. The following conclusions can be drawn:

(1) The breakouts of concrete blocks dominate the failure mode of PBLs in tension. The tensile capacity of PBLs is lower than half of the corresponding shear capacity. The peak separation is around 1 mm. When the applied tensile force is no larger than 0.3 times the tensile capacity, the residual separation is negligible.
(2) Based on the parametric study, the embedded depth is the major factor in the tensile performance of PBLs. The tensile capacity mainly increases with the embedded depth and the concrete strength.
(3) The hole diameter performs significant impacts on the tensile stiffness because the hole dimension directly affects the contact area between hole walls and concrete dowels at the early loading stage. The tensile stiffness is also influenced by the embedded depth when the embedded depth is smaller than 100 mm.
(4) In the proposed equations, the tensile capacity of PBLs is related to the embedded depth, hole diameter, and concrete strength. As regards the tensile stiffness, the influential factors are the embedded depth, hole diameter, and concrete modules.

## 6. Future works

Since shear connectors are usually designed to undertake considerable shear forces, the combined shear-tensile response and even the mixed shear-tensile-lateral behavior of PBLs should be revealed and analyzed. Additional experimental and analytical studies for the structural behavior of PBLs under complex load combinations will be presented in the future works. Besides, the effects of the number of holes on the tensile behavior and the related analytical expressions should be investigated in detail.

## Declaration of Competing Interest

The authors declare that they have no known competing financial interests or personal relationships that could have appeared to influence the work reported in this paper.

## References


[1] Liu Y, Xin H, Liu Y. Load transfer mechanism and fatigue performance evaluation of suspender-girder composite anchorage joints at serviceability stage. J. Constr. Steel Res. 2018;145:82–96.
[2] Liu R, Liu Y. Analysis of auxiliary ribs in steel-concrete joint of hybrid girder. J. Constr. Steel Res. 2015;112:363–72.
[3] Wang S, He J, Liu Y, Li C, Xin H. Shear capacity of a novel joint between corrugated steel web and concrete lower slab. Constr. Build. Mat. 2018;163:360–75.
[4] Zhu Y, Nie X, Fan J, et al. Experimental and analytical investigation on pull-out performance of multihole thin-rib perfobond connectors. J. Bridge Eng. 2019;24 (5):04019037.
[5] Zheng S, Liu Y, Xu H. Structural analysis of steel bracket-concrete walls in cable-tower composite anchorage. Eng. Mech. 2014;31(5):197–202 (in Chinese).
[6] Kim YH, Kang JY, Koo HB, Kim DJ. Pull-out resistance capacity of a new perfobond shear connector for steel pile cap strengthening. Adv. Mat. Sci. Eng. 2016:1–12.
[7] Zheng S, Liu Y. Experiment of initial shear stiffness of perfobond connector. China J. Highw. Transp. 2014;27(11):69–75.
[8] Zheng S, Liu Y, Yoda T, Lin W. Parametric study on shear capacity of circular-hole and long-hole perfobond shear connector. J. Constr. Steel Res. 2016;117:64–80.
[9] Liu Y, Xin H, Liu Y. Experimental and analytical study on shear mechanism of rubber-ring perfobond connector. Eng. Struct. 2019;197:109382.
[10] Liu Y, Wang S, Xin H, Liu Y. Evaluation on out-of-plane shear stiffness and ultimate capacity of perfobond connector. J. Constr. Steel Res. 2019;105850.
[11] Code for Design of Concrete Structures (GB 50010-2010). China Building Industry Press, Beijing, China, 2010.
[12] CEB-FIP Model Code 2010, British Standard Institution, 2010.
[13] ABAQUS Documentation. Version 6.12. Dassault system, USA, 2012.
[14] Nguyen HT, Kim SE. Finite element modeling of push-out tests for large stud shear connectors. J. Constr. Steel Res. 2009;65(10–11):1909–20.
[15] P.J. McMackin, R.G. Slutter, J.W. Fisher. Headed steel anchors under combined loading, Eng. J. AISC 1973 (Second Quarter) 43–55.
[16] PCI design handbook: precast and prestressed concrete, 5th Ed., Precast/ Prestressed Concrete Institute (PCI), Chicago (IL), 1999.
[17] ACI 318-08, Building code requirements for structure concrete and commentary, American Concrete Institute, Farmington Hills (MI), 2008.
[18] Fuchs W, Eligehausen R, Breen JE. Concrete capacity design approach for fastening to concrete. Struct. J. ACI 1995;92(1):61–88.
[19] R.D, Force at a point in the interior of a semi-infinite solid, Physics 7(5) (1936) 195–202.